Icarus 452 (2026) 117022

Contents lists available at ScienceDirect

Icarus

journal homepage: www.elsevier.com/locate/icarus

Research Paper

Retention of water ice in lunar permanent shadowed regions

Sunpeng Zhou [a,b,1], Zhenpeng Wang [a,b,1], Shanshan Zhou [a,b], Hang Deng [a,b], Qinggong Wang [c], Rui Wu [d], Wei Yao [e], Ke Xu [a,b,*]

[a] Department of Energy and Resources Engineering, School of Mechanics and Engineering Science, Peking University, Beijing 100871, China
[b] Research Institute of Extraterrestrial Material, Peking University, Beijing 100871, China
[c] School of Energy and Environmental Engineering, University of Science and Technology Beijing, Beijing 100083, China
[d] School of Mechanical Engineering, Shanghai Jiao Tong University, Shanghai 200240, China
[e] Qian Xuesen Laboratory of Space Technology, China Academy of Space Technology, Beijing 100094, China

ARTICLE INFO

Keywords:
Lunar ice
Cold trap
Permanent shadowed region

ABSTRACT

Lunar polar regions are considered promising areas where massive water resources may exist, especially in the permanently shadowed regions (PSRs) where ice can hardly evaporate once formed due to the extremely low temperature. Here we estimate the ice retention by simulating the evolution of potential water ice reserves in PSRs in up to one billion years based on a simple numerical model. Dissipation at the warmer edge of PSRs and vapor supply from lower latitudes are identified as major mechanisms of ice spatial distribution evolution. We investigate the effects of PSRs sizes, boundary temperature, initial ice saturation, effective diffusion coefficient, the water vapor influx, and the reflected / scatted solar radiation from crater wall. Major findings include:

1. In large cold traps (radius greater than 20 m), most initially trapped water ice can be preserved, that may serve as major water supply for human activity; in micro cold traps (radius smaller than 1 m), water ice may only remain temporarily.
2. Mixing between ice in shallow regolith and in deep regolith in PSRs is very limited, which can be utilized for investigating their distinct geological origins.

This approach can also be extended to study other volatiles on extraterrestrial bodies in cold traps.

1. Introduction

Recent explorations imply the presence of exploitable water ice resources in the permanently shadowed regions (PSRs) at lunar polar regions (Colaprete et al., 2010; Li et al., 2018; Rubanenko et al., 2019). There may be up to 10 wt% water ice within 10 m below the lunar surface in PSRs, and the total mass of water ice on the Moon is estimated to be up to billions of tons (Cannon et al., 2020; He et al., 2023; Rubanenko et al., 2019). Abundant water ice reserves may allow large-scale in-situ extraction, which could fundamentally satisfy the need of water resource for future lunar stations' construction, operation, and industrialization. Cold traps with radius greater than 100 m are usually categorized as areas with potential extraction value (Rubanenko, 2024). Meanwhile, micro-cold traps are of larger numbers and easier to reach, and may also contain water ice reserves with scientific significance (Hayne et al., 2021). Past and future missions — including LRO, LCROSS, Chandrayaan-2, the Artemis Program, and Chang'e — are dedicated to identifying water ice reservoirs in the lunar polar region, with Chang'e-7 specifically targeting Shackleton Crater. (Angelopoulos, 2011; Bandfield et al., 2015; Colaprete et al., 2010; Goswami and Annadurai, 2011).

Despite extensive remote sensing data and laboratory research, the origin of existing water ice on the Moon remains under debate. The three most widely accepted sources of polar water ice on the Moon include: 1) impacts from ice-bearing asteroids and comets, 2) transient atmosphere during volcanic outgassing, and 3) production of solar wind–mineral reactions (Arnold, 1979; Cannon et al., 2020; Crider and Vondrak, 2003; Luchsinger and Chanover, 2022; Ong et al., 2010; Stewart et al., 2011). In addition, water molecules migrate from low-latitude areas toward high-latitude cold traps via ballistic hopping (Cannon et al., 2020; Chen

* Corresponding author.
E-mail address: kexu1989@pku.edu.cn (K. Xu).
[1] These two authors contribute equally to this paper.

https://doi.org/10.1016/j.icarus.2026.117022
Received 7 November 2025; Received in revised form 13 February 2026; Accepted 27 February 2026
Available online 3 March 2026

et al., 2025; Luchsinger and Chanover, 2022; Moores, 2016; Watson et al., 1961). Water ice delivered by impactors may ultimately remain as a uniformly mixed component within the regolith over relatively short timescales. In contrast, water ice formed from solar wind, transient atmosphere and ballistic water vapor influx may form an ice-rich, shallow regolith layer by the gardening effect.

Estimating the total extractable water ice in a cold trap is an important but challenging task. Water ice reserves in a specific cold trap m_{water} can be estimated as:

$$m_{water}(t) = M_i \cdot \eta(t, \mathrm{R}_c, \ldots) \quad (1)$$

where M_i is the total initial mass of ice in the cold trap, and t is the time after cold trap formation. Geological parameters that determine these parameters typically include the size of the cold trap R_c, boundary conditions, regolith transport properties, influx rate, etc.

In Eq.1, previous research has focused more on M_i (Arnold, 1979; Cannon et al., 2020; Costello et al., 2020; Ong et al., 2010; Stewart et al., 2011), with extensive investigations conducted on the age of impact craters as cold traps, the relationship between crater and impactor size, and the retention of water vapor at the moment of impact (Ong et al., 2010; Spudis et al., 2008; Stewart et al., 2011). However, there has been a lack of corresponding studies on retention rate η, leaving the key question unsolved: how much water ice can remain retained over geological timescales, that may be utilized in humanity's future lunar missions?

Dissipation of water ice after their formation includes direct escape into space from the regolith surface, and horizontal migration of vapor into warmer non-PSR regions which ultimately also escape into space. This process is through multiple evaporation – molecular diffusion - condensation cycles in porous regolith. Its governing equations are mathematically similar to the ripening and dissolution of dispersed fluid in the subsurface aquifer (de Chalendar et al., 2019; Feng et al., 2022; Li et al., 2020; Yu et al., 2023), but distinct Knudsen diffusion mechanism should be considered (Schieber et al., 2022). Previous predictive models typically simply considered vertical transport and neglected the horizontal temperature gradient, which can also drive vapor escape (Rubanenko and Aharonson, 2017; Siegler et al., 2015). Moreover, these studies typically estimated the local vapor pressure as the saturation pressure at the local temperature to derive mass transfer rates. This approach, however, overestimates the vapor pressure in regions that are dry or devoid of water ice (Danque and Cannon, 2024).

Influx is mainly from water vapor flux originating from low latitudes, and is subject to significant uncertainty, with previous studies estimating the range of solar wind-induced influx to be between 2.93×10^{-5} kg·m^{-2}·Gyr^{-1} and 0.38 kg·m^{-2}·Gyr^{-1} (Huang et al., 2022; Jones et al., 2018), and the range of low-latitude water vapor influx to be between 5.68×10^{-2} kg·m^{-2}·Gyr^{-1} and 4.1×10^{3} kg·m^{-2}·Gyr^{-1} (Crider and Vondrak, 2000, 2003; Grant et al., 1991; Schorghofer and Taylor, 2007; Stewart et al., 2011). Influx history can also provide valuable information about the early-time behaviors of the solar system. Although volcanic activity and the resulting transient atmospheres may have been a significant source of water ice in cold traps, the period of peak lunar volcanism occurred between 4 and 2 Ga (Head et al., 2020; Luchsinger and Chanover, 2022; Wilcoski et al., 2022). Therefore, it does not serve as a mechanism for the influx of water vapor from the lunar surface into cold traps under present-day conditions and within the timeframe simulated in this study.

In this paper, we establish a preliminary model to resolve function $\eta(t, R_c, \ldots)$ at different geological conditions to predict the retention rate of exogenous water ice in PSRs. With this model, we aim to:

1) identify key parameters that determine water ice evolution in a cold trap;
2) evaluate the water reserves in typical cold traps, and provide a rough criterion to predict whether ice in a trap is of value for massive water extraction;
3) identify potential connections between historical water influx rates from lower latitudes to PSRs and current features of the PSRs, which may help to reveal the interaction history between lunar and other solar system bodies.

2. Numerical modeling

2.1. Computational domain setup

As shown in Fig. 1, we simulate the migration of water ice within the regolith of PSRs in high-latitude lunar craters over geological timescales. The cold traps receive no direct solar illumination; they are heated only by reflected and scattered thermal radiation from the crater rim and cool via thermal emission. Water ice inside the PSR may escape as vapor from the surface or subsurface edges, while the surface may also receive water vapor influx from other regions of the Moon.

The PSR is located on the floor of the crater, where the subsurface regolith is a porous medium with a thickness denoted by h and measured to be 10 m (Rubanenko et al., 2019). Given that the depth-to-diameter ratio of such craters is generally below 0.2 (Wu et al., 2022) and the floor elevation varies relatively little, the PSR can be reasonably approximated as a cylinder for computational simplicity. Since the PSR occupies the primary area at the center of the crater (Song et al., 2021), the radius of the cylinder (R_c) is approximated to equal the crater radius.

A certain amount of water ice is initially buried within the PSR. We aim to calculate the distribution and the retention fraction (η) over geological time. Our simulation covers the time span from 1 Ga to the present. This period is selected because the area of lunar PSRs has varied over time due to the polar axis deflection in the Moon's history (Siegler et al., 2011). As a reference, the site of the artificial impact in Cabeus crater has been in permanent shadow only since about 0.9 Ga ago (Schörghofer and Rufu, 2023).

2.2. Key assumptions and simplifications

Numerical simulations require systematic simplification to achieve an acceptable computational cost and ensure computational stability.

2.2.1. Heat transfer quasi-steady state assumption

We compare the characteristic times governing mass diffusion and heat conduction. The mass transfer is through Knudsen diffusion process of water vapor in an extreme vacuum environment, with a characteristic time on the order of 10^{22}–10^{25} s. In contrast, the heat transfer process is dominated by thermal conduction within the lunar regolith, with a characteristic time of less than 10^{9}–10^{10} s, indicating that heat transfer is significantly faster than mass transfer. Additionally, the thermal relaxation time associated with the latent heat during phase change is less than 10^{10}–10^{12} s, which is also negligible compared to the characteristic timescale of mass transfer. Detailed computational procedures are provided in Supplementary Material S2. Therefore, to simplify the computation, we treat the heat transfer process as reaching a steady state within a single time step, thereby decoupling the two processes. It is important to emphasize that this does not imply that the heat transfer is truly in a steady-state condition, because the thermal conductivity within the computational domain changes as the spatial distribution of ice evolves.

2.2.2. Binary-regions assumption

For computational stability, at the beginning of each time step we divide the computational domain into ice-bearing regions and dry regions based on an ice saturation fraction threshold ($S = 10^{-10}$, S is the ice saturation, i.e. ice volume fraction in void space). In the ice-bearing regions, water vapor and ice are in phase equilibrium. Accordingly, the

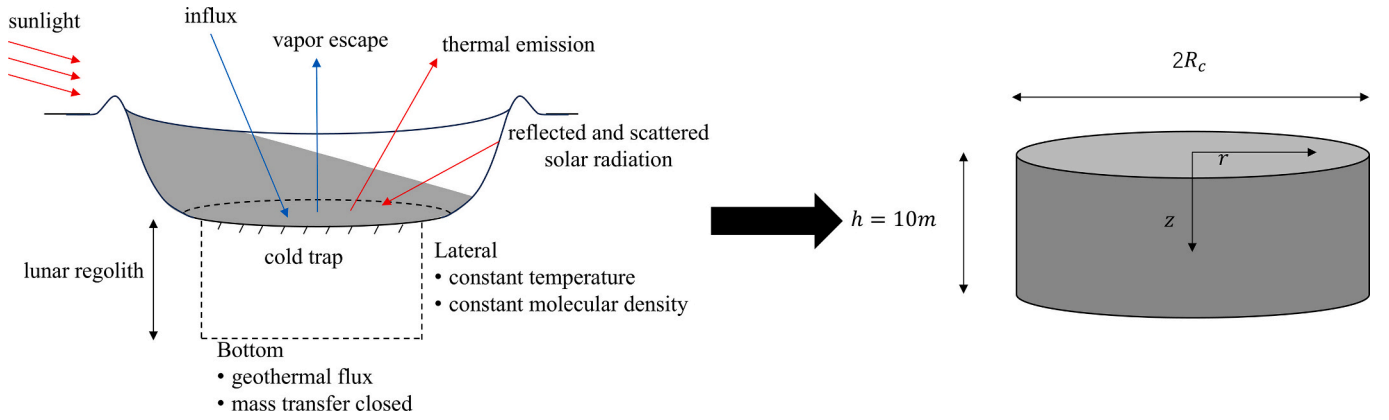

Fig. 1. Schematic of the geometric setup of cold trap with boundary conditions (left) and the two-dimensional cylindrical coordinate system for simulation (right).

water vapor partial pressure is determined by phase equilibrium, set equal to the saturation vapor pressure P_s corresponding to the local temperature (Siegler et al., 2015). In the dry regions, S is explicitly set to zero, and the water vapor pressure P_{water} is treated as an independent variable determined by the vapor diffusion dynamics. A transition rule is enforced: if the calculated P_{water} exceeds P_s in dry regions, the node is immediately switched to the ice-bearing region.

2.2.3. Mass transfer quasi-steady state in dry regions

In dry regions, mass transfer is dominated by water vapor diffusion, with a characteristic time on the order of 10^2–10^3 s (Detailed computational procedures are provided in Supplementary Material S2). This is significantly shorter than the characteristic time for mass transfer in ice-bearing regions (10^{22}–10^{25} s). Consequently, it is safe to assume that the water vapor in dry regions reaches a steady state at each time step, shaped only by boundary conditions and adjacent ice-bearing region status.

2.2.4. Heat transfer is dominated by thermal conduction

Due to the extremely rarefied nature of the water vapor, its ability to carry and transfer thermal energy can be neglected, consequently, convective heat transfer can be disregarded. As for radiative heat transfer, its equivalent thermal conductivity can be calculated as $\sigma\varepsilon T^3 l_p$ (where σ is the Stefan-Boltzmann constant, ε is the surface emissivity, T is the temperature, and l_p is the characteristic heat transfer length scale, taken as the mean particle size of the lunar regolith; see Table 1 for specific parameters). The resulting value ranges from 10^{-5} to 10^{-7} W/(m·K), which is significantly lower than the thermal conductivity of the lunar regolith (~10^{-2} W/(m·K) (Grott et al., 2010)). Thus, radiative heat transfer within the regolith can also be justifiably neglected. However, the thermal emission from the cold trap surface to space cannot be ignored.

2.2.5. Neglect of gravity and surface energy

In conventional modeling of multiphase flow through porous media, gravity and surface energy are typically considered key driving forces for mass transfer (Krevor et al., 2015; Xu et al., 2019). However, under the extreme thermal conditions of the lunar cold trap, the change in the molar Gibbs free energy (i.e., chemical potential μ) of water vapor—which, due to phase equilibrium, is equal to that of water ice—induced by temperature gradients is orders of magnitude greater than the contributions from gravitational potential differences and surface energy. Therefore, the effects of gravity and surface energy on mass transfer are considered negligible and are not included in the present model. Detailed computational procedures are provided in Supplementary Material S3.

Table 1
Parameters adopted for our model.

Parameter	Symbol	Value	Reference
Characteristic length (regolith particle size)	l_p	~10^{-4} m	Heiken et al. (1991)
Tortuosity	τ	1–2	Schieber et al. (2021)
Density of ice	ρ_i	932 kg•m^{-3}	Daucik and Dooley (2011)
Bulk density of the lunar regolith	$\rho_{regolith}$	1600 kg/m^3	Fa (2020)
Initial water ice saturation	S_{init}	0.1%–10%	Arnold (1979); Colaprete et al., 2010; Rubanenko and Aharonson (2017); Schultz et al. (2010); Stewart et al. (2011)
Internal heat flow	q_0	0.0049 W/m^2 0.018 W/m^2	Wei et al. (2023); Langseth et al. (1976a)
The number density of external atmospheric molecules	n_e	5 × 10^{5}molecules/m^3	Heiken et al. (1991)
Water vapor flux toward regolith surface	J_{in}	5.7 × 10^{-2} kg·m^{-2}·Gyr^{-1} to 4.1 × 10^3 kg·m^{-2}·Gyr^{-1}	Stewart et al. (2011); Heiken et al. (1991)
Water vapor influx minus space weathering loss	$J_{in,net}$	0 kg·m^{-2}·Gyr^{-1} to 4.1 × 10^3 kg·m^{-2}·Gyr^{-1}	
Stefan-Boltzmann constant	σ	5.67 × 10^{-8} W•m^{-2}•K^{-4}	
Surface emissivity	ϵ	0.95	Bandfield et al. (2015); Logan et al. (1972)
Radiative flux from crater wall	q_{wall}	0.86–4.83 W•m^{-2}	Supplementary materials S6; Hayne et al. (2017)
Temperature of the lateral boundary	$T_{boundary}$	120-160 K	Williams et al. (2019); Zhong et al. (2023)
Cold trap radius	R_c	1 cm-10 km	Halim et al. (2021); Hayne et al. (2021)

2.2.6. Assumption of a uniformly mixed top layer and frost layer

An excessive influx of water vapor may lead to the formation of an ice frost layer on the surface of the cold trap, where it can be preserved due to the persistently low temperatures. However, impact gardening from micrometeorite bombardment and other processes enables material to be buried below the surface (Costello et al., 2018). We assume that the top half-meter of regolith has been thoroughly mixed over geological timescales (Cannon et al., 2020), resulting in a uniform ice

saturation (S) within this layer (S can vary in the r direction). If the influx of water molecules entering the cold trap is sufficiently high, the water ice content in the surface layer may exceed its storage capacity. When S exceeds a threshold value of 0.8 (which we take as the maximum packing or retention capacity of the soil when saturated), the vapor influx can no longer effectively penetrate the surface layer and instead condenses as a frost layer on the cold trap surface.

2.3. Governing equations and boundary conditions

Based on the assumptions and simplifications outlined in Section 2.2, we have established the following governing equations to simulate the evolution of subsurface water ice within a 10-m-deep regolith column in the cold trap from 1 Ga to the present. The simulation is conducted in a two-dimensional cylindrical coordinate system (see Fig. 1). The finite-volume discretization scheme and the verification of grid independence are detailed in Supplementary Materials S4 and S5, respectively. Under the quasi-steady-state assumption for heat transfer, the heat and mass transfer equations are decoupled.

Heat transfer is treated as reaching a steady state at each computational time step.

$$\nabla\cdot(K\nabla T) = 0 \tag{2}$$

where K denotes the thermal conductivity of the ice-bearing lunar regolith or the dry regolith, and T is the temperature.

To rigorously account for both pressure-driven diffusion and thermodiffusion (temperature-driven diffusion), we characterize the molar Gibbs free energy of the water component using the chemical potential (μ). The gradient of the chemical potential drives the water vapor flux. Building upon earlier work concerning subsurface dispersed fluid evolution (Xu et al., 2019), we develop a mass transfer Darcy-scale continuum model. The specific derivation of the formula is provided in Supplementary Material S1.

For mass transfer, we solve the distinct conservation equations for the ice-bearing region and the dry region, respectively:

$$\frac{\partial(S\rho_i + (1-S)\rho_v)}{\partial t} = \nabla\cdot\left(\frac{(D/\tau)\rho_v}{RT}\nabla\mu\right), if\ S > 10^{-10} \tag{3}$$

$$0 = \nabla\cdot\left(\frac{D\rho_v}{RT}\nabla\mu\right), if\ S < 10^{-10} \tag{4}$$

where t is time, R is ideal gas constant, ρ_i is the density of ice (Table 1), ρ_v is the density of water vapor (calculated using the ideal gas equation, $P_{water}M/RT$, M is molar mass of water, 0.018 kg·mol^{-1}), S is the ice saturation (ice volume fraction in void space), D is the water vapor diffusion efficient, and τ the tortuosity (the ratio of the actual diffusion path length of molecules in lunar regolith to the apparent distance) (Schieber et al., 2021; Zheng et al., 2013).

The chemical potential (μ) of the water component is expressed as follows. Due to phase equilibrium, the chemical potential of water ice equals that of water vapor. The detailed derivation of this formula is provided in Supplementary Material S1.

$$\mu = \mu^0 + RTln\frac{P_{water}}{P_0} + S_e^0(T - T_0) - C_p\left(Tln\frac{T}{T_0} + T_0 - T\right) \tag{5}$$

This expression defines the chemical potential as a function of partial water vapor pressure (P_{water}) and temperature (T). Here, μ^0 and S_e^0 are the reference chemical potential and entropy, respectively, at the reference state (at $T = T_0$ and $P_{water} = P_0$, $T_0 = 273.16$ K is the reference temperature, and P_0 is the saturated vapor pressure when $T = T_0$, 611.73 Pa). In addition, $C_p = (1 + f/2)R$ represents the specific heat capacity at constant pressure for an ideal gas composed of polyatomic molecules, where f denotes the number of molecular degrees of freedom. For a water molecule, $f = 6$, comprising three translational and three rotational degrees of freedom.

Initial condition. We assume that the water ice content within the regolith is initially uniform, resulting from impact gardening processes. Impactors, categorized as comets or asteroids based on composition, determine the mass of water delivered to the Moon (Ong et al., 2010). The size of these impactors can be inferred from associated crater morphology (Ivanov, 2001), and the formation age of a specific area can be revealed through crater counting (Spudis et al., 2008). Combining these parameters allows for the preliminary estimation of the total water ice delivered. Existing studies generally establish that the thickness of the loose regolith is approximately 10 m, with the water ice content typically ranging from 0.1 wt% to 10 wt% (Arnold, 1979; Colaprete et al., 2010; Rubanenko and Aharonson, 2017; Schultz et al., 2010; Stewart et al., 2011). Considering that the densities of ice (ρ_i) and lunar regolith ($\rho_{regolith}$, Table 1) are not significantly different, the initial saturation of the system is also set to a uniform value (S_{init}), ranging from 0.1% to 10%.

Additionally, since we have provided the heat transfer quasi-steady state assumption, the calculation does not require the specification of thermal initial conditions. The initial temperature field is obtained by solving the steady-state heat transfer equation with the initial saturation distribution.

The boundary conditions are illustrated in Fig. 1.

2.3.1. Bottom boundary

At the bottom of the regolith domain, heat transfer is dominated by the geothermal flux. Prior studies have established the critical importance of quantifying this internal heat flow q_0 as Table 1. Concurrently, this boundary is treated as closed with respect to mass transfer.

The bottom boundary conditions are specified as follows:

$$K\frac{\partial T}{\partial z}|_{z=h} = q_0 \tag{6}$$

$$\frac{\partial \mu}{\partial z}|_{z=h} = 0 \tag{7}$$

2.3.2. Axis of symmetry ($r = 0$)

Due to the axial symmetry of the problem, a zero-flux (Neumann) condition is applied for all variables:

$$\frac{\partial T}{\partial r}|_{r=0} = 0 \tag{8}$$

$$\frac{\partial \mu}{\partial r}|_{r=0} = 0 \tag{9}$$

2.3.3. Lateral boundary

Existing studies indicate that although the lunar regolith within several centimeters of the surface experiences extreme diurnal temperature variations, the low thermal conductivity of the surface regolith means that temperatures at a certain depth underground remain unaffected by surface illumination conditions (Heiken et al., 1991; Vasavada et al., 1999; Zhong et al., 2023). Furthermore, geothermal influence is negligible (Zhong et al., 2023). Therefore, we can reasonably consider the outer boundary of the cold trap to be at a constant temperature, $T_{boundary}$. Additionally, due to the high temperatures present, we assume the exterior region beyond the boundary is a dry region. Therefore, we also specify this boundary as having a water molecular density n_e (Table 1), set to a value in equilibrium with the lunar exosphere—hence it is a constant independent of the water molecule influx based on published data (Heiken et al., 1991). Although the water vapor density in the exosphere above the cold trap varies with the influx, we assume that the incoming molecules possess a net downward velocity and thus do not establish a local equilibrium.

The lateral boundary conditions are specified as follows:

$$T|_{r=R_c} = T_{boundary} \tag{10}$$

$$P_{water}(r = R_c) = n_e/(k_B T) \tag{11}$$

where k_B is the Boltzmann constant. The chemical potential at the boundary is calculated by substituting this pressure and temperature into Eq. 5.

2.3.4. Upper boundary

The upper boundary of the cold trap is in contact with the lunar exosphere. We neglect conductive heat transfer at this boundary, and consider only radiative heat transfer since the temperature difference between the regolith surface and space background is sufficiently large. The radiative term q_{rad} includes the surface's thermal emission and the solar radiation reflected or scattered from the crater rim q_{wall}. Specific calculations of q_{wall} can be found in the Supplementary Materials S6. Therefore, a radiation term is present on the surface:

$$\nabla\cdot(K\nabla T)|_{z=0} = -q_{rad} \tag{12}$$

$$q_{rad} = -\sigma\epsilon T^4 + q_{wall} \tag{13}$$

The values adopted are reported in Table 1.

For mass transfer boundary condition on upper surface, water molecules migrate from the subsurface to the surface layer and escape, while the lunar exosphere also experiences an influx of water molecules from lower latitudes (Moores, 2016). For the net surface flux J_{net}, we define it as the difference between the external influx $J_{in,net}$ and the molecular leakage J_{out}. Here, $J_{in,net}$ represents the flux of water molecules arriving above the cold trap from lower latitudes via the lunar exosphere J_{in}, minus the loss due to space weathering at the surface (Farrell et al., 2019; Morgan and Shemansky, 1991). J_{out} denotes the flux of water vapor escaping from the cold trap surface, originating from the sublimation of subsurface ice. The upper boundary conditions are specified as follows:

$$\frac{(D/\tau)\rho_v}{RT}\frac{\partial\mu}{\partial z}|_{z=0} = -J_{net} \tag{14}$$

$$J_{net} = J_{in,net}\Big/\phi_{solid} - J_{out} = J_{in,net}\Big/\phi_{solid} - \frac{1}{4}\frac{P_{water}}{RT}\nu M \tag{15}$$

where $\nu = \sqrt{8RT/\pi M}$ is the mean molecular speed and ϕ_{solid} is the lunar regolith porosity. The reason for dividing the influx by porosity is that Eq. 3 itself already results from dividing both sides of the equation by porosity (see Supplementary Material S1). $J_{in,net}$ is critical for the accumulation of water ice in the cold trap. Based on previous studies of the continuous accumulation process caused by comet impacts (Stewart et al., 2011), we estimate the upper limit of the water vapor influx J_{in} to be 4.1×10^3 kg·m^{-2}·Gyr^{-1}. The lower limit is derived from prior measurements of water molecule density in the lunar surface environment (Heiken et al., 1991), which is 5.68×10^{-2} kg·m^{-2}·Gyr^{-1}. However, it remains challenging to estimate the losses in the lunar regolith surface layer caused by space weathering (Farrell et al., 2019; Morgan and Shemansky, 1991). Therefore, the lower limit of $J_{in,net}$ is estimated as 0.

2.4. Key parameters and variables

The parameters and variables intrinsic to the governing equations exhibit strong dependence on local temperature (T) and ice saturation (S). To solve the model, we must define the functional forms for the thermal conductivity (K), the diffusion coefficient (D), and the saturated vapor pressure (P_s).

2.4.1. Thermal conductivity K

The thermal conductivity represents the effective thermal conductivity of the ice-bearing lunar regolith mixture. It is thus inherently dependent on both the ice saturation (S) and the inter-particle bonding modes between the ice crystals and the solid regolith grains (Siegler et al., 2012). Given the low water-ice content in lunar regolith and temperature-constrained low saturation vapor pressure, we adopt a simplified approach based on a volume mixing law dominated by point-contact interactions between the ice and soil components:

$$K = K_{solid} + S\cdot\phi_i\cdot K_i \tag{17}$$

where K_{solid} is the thermal conductivity of a granular packing of lunar regolith grains, which depends on both how the grains are in contact with each other and the intrinsic thermal conductivity of the grains themselves (K_s), K_i is the thermal conductivity of ice crystals, and ϕ_i is the porosity of water ice structures (such as frost on the surface of lunar soil particles. K_{solid} is determined by their mechanical properties (Parzinger, 2014; Reiss, 2018), while K_i is determined by temperature (Ratcliffe, 1962):

$$K_{solid} = 3.44(1-\phi_{solid})^{\frac{4}{3}}\left(\frac{1-\nu_p^2}{Y}\right)^{\frac{1}{3}}K_s P_{compress}^{\frac{1}{3}} \tag{18}$$

$$K_i = \left(\frac{7.8}{T} - 0.00615\right)\cdot 100 \tag{19}$$

where ϕ_{solid} is the porosity of the lunar regolith particle packing, $\nu_p = 0.3$ is Poisson's ratio, $Y = 80$ MPa is Young's modulus of the solid particle, and $P_{compress} = \rho_{regolith} g z$ is the load that compresses the particles, where g is gravitational acceleration (1.62 m·s^{-2}) and z is the depth. The value of K_s varies with temperature and rock type (Reiss, 2018; Woods-Robinson et al., 2019), and it ranges from 2 to 10 W/(m·K) between 100 and 400 K. Considering that its variation is relatively small compared to the thermal conductivity of ice, we set this as the constant 3.49 W·m^{-1}·K^{-1}, which is the thermal conductivity of basalt. Additionally, the temperature (T) mentioned here is in Kelvin units, and the units of K_{soild} and K_i are W/(m·K). At a depth of 2 cm, the calculated conductivity is 0.03 W/(m·K), which is consistent in magnitude with values reported in the literature (Grott et al., 2010; Langseth et al., 1976b). For deeper regolith, our formulation suggests that thermal conductivity increases as interparticle contact becomes tighter, but this lacks validation against data from the depths of permanently shadowed regions.

Typical values of ϕ_{solid} for lunar regolith range from 0.44 ± 0.02 to 0.52 ± 0.02, including both inter- and intra-granular porosity, as calculated from the depth-dependent bulk density measured in situ during the Apollo missions (Heiken et al., 1991). We set $\phi_{solid} = 0.5$ in this article. Furthermore, we assume that the porosity of water ice ϕ_i is similar to that of lunar soil particles, without changing their porosity. Therefore, ϕ_i is also equal to 0.5.

As shown in Fig. 2 (a), the ice saturation is a critical factor in calculating the thermal conductivity of lunar regolith.

2.4.2. Frost layer alters the thermal conductivity of the top regolith layer

If the water ice saturation in the uniformly mixed top layer exceeds 0.8, a frost layer forms at the surface. Under this condition, the effective thermal conductivity of the composite layer is calculated as the series combination of the ice-bearing regolith and the overlying frost layer (Levenspiel, 2014).

$$K = \frac{(h_{regolith} + h_{frost})\cdot\phi_i\cdot K_i\cdot K_{saturated}}{h_{regolith}\cdot\phi_i\cdot K_i + h_{frost}\cdot K_{saturated}} \tag{16}$$

where $h_{regolith} = 0.5$ m is the depth of the top layer, h_{frost} is the height of the frost on the regolith surface, $K_{saturated}$ is the thermal conductivity of the saturated regolith ($S = 0.8$). The height of the frost, h_{frost}, is determined by the mass of accumulated water ice at the surface (excluding that mixed with the regolith), the density of water ice (ρ_i), and the porosity of the water ice structures (ϕ_i, taken as 0.5).

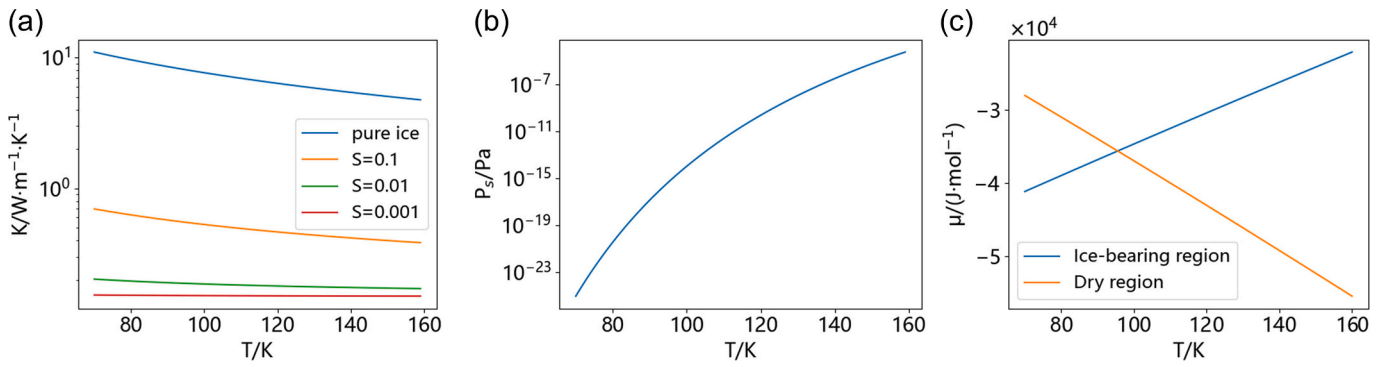

Fig. 2. Key physical property parameters varying with temperature. (a) Thermal conductivity of pure ice and ice-bearing lunar regolith with different saturation levels. (b) Equilibrate vapor pressure. Note that it is very sensitive to temperature. (c) The chemical potential of water vapor in the ice-bearing region, and in the dry region under external atmospheric molecule density shown in Table 1.

2.4.3. *Diffusion coefficient D*

n lunar regolith, $Kn >> 10$, so we adopt the Knudsen diffusion coefficient (Reinecke and Sleep, 2002), which can be calculated as:

$$D = \frac{1}{3} v l_p \tag{17}$$

The parameter values adopted are reported in Table 1. Therefore, the effective diffusion coefficient depends on the average particle size of the lunar regolith l_p divided by the porous media tortuosity τ. The tortuosity typically ranges from 1 to 2 (Schieber et al., 2021).

2.4.4. *Saturated vapor pressure P_S*

The saturated water vapor pressure is a function of temperature, and it is calculated using the empirical equation (Daucik and Dooley, 2011):

$$P_s = P_0 \exp(\alpha / T^*) \tag{18}$$

Where $T^* = T/T_0$ is the dimensionless temperature, and $\alpha = -21.2\ T^{*0.00333} + 27.3\ T^{*1.21} - 6.11\ T^{*1.7}$. The formula demonstrates that a decrease in temperature can reduce the saturation vapor pressure of water ice by orders of magnitude, thereby also lowering the sublimation rate. For individual water molecules, this is equivalent to an exponential increase in their average adsorption time on the ice surface (Schorghofer and Taylor, 2007). Consequently, lower temperatures significantly slow down the diffusion rate of water ice (Schörghofer, 2025).

As shown in Fig. 2 (b), in the deep low-temperature regime, the magnitude of the saturated vapor pressure of ice crystals changes drastically with temperature. Consequently, even minor local temperature differences can establish a significant pressure gradient capable of driving mass transfer. This sensitivity leads to conditions, as shown in Fig. 2 (c), where the chemical potential of water vapor in potentially dry regions can exceed that within the ice-bearing lunar regolith when the local temperatures are sufficiently low.

3. Results

We first examine the evolution of water ice in a demonstrative micro cold trap, followed by an investigation into the influence of geothermal flux (q_0), lateral boundary temperature (T_{boundary}), initial saturation (S_{init}), cold trap size (R_c), effective diffusion coefficient, net surface water vapor influx ($J_{\text{in,net}}$), and radiative flux from crater wall (q_{wall}), on the resulting ice evolution.

3.1. *Evolution in a demonstrative micro cold trap*

A significant portion of the cold trap area on the Moon is concentrated in micro cold traps smaller than 1 km (Hayne et al., 2021). Given this prevalence, and to avoid complexities associated with heterogeneity that arise in larger domains, we focus our initial analysis on a representative small-scale system. Specifically, we examine a micro cold trap characterized by a 10-m diameter and 10-m depth. The thermal boundary condition is held constant at 160 K, slightly above the reported Shackleton crater rim temperatures of 120–156 K (Zhong et al., 2023). Furthermore, this also corresponds to the typical annual mean temperature in high-latitude regions (Paige et al., 2010; Williams et al., 2019). Initial conditions specify a 0.5% saturation. The radiative flux from the crater wall is set to 2.63 W/m^2. The lunar geothermal heat flux is set to 0.018 W/m^2 (Langseth et al., 1976a). The value of the average lunar regolith particle size divided by the tortuosity is set to 10^{-4} m. Under the assumption that space weathering balances the influx of water molecules, $J_{\text{in,net}}$ is taken as 0. The primary objective is to determine the resulting water ice distribution after an evolutionary timescale of one billion years.

The temperature and ice saturation field evolution are shown in Fig. 3 (a)-(f). The boundary of the ice-bearing region (ice front) retreats faster in the deep layer than in the surface layer. This non-uniform front movement is a result of the non-uniform temperature field in the vertical direction, which is shaped by the radiative cooling upper surface and weakly heating bottom boundary. We note that the majority of ice loss occurs through the lateral boundary and dissipation from upper boundary is negligible, although the upper boundary area is comparable to that of literal boundary.

We further observe that the maximum water-ice saturation is located near the ice front within the ice-bearing region. This is attributed to the positive correlation between the chemical potential and temperature in the ice-bearing region (Fig. 2 (c)), which drives water ice at the ice front continuously transports mass inward (as illustrated in Fig. 3 (g)).

Fig. 3 (h) plots the variation of the ratio (η) of water ice content in the cold trap to the initial water ice mass over time. The dissipation becomes slower during the 1 billion years, and 81% of total initial water ice can be preserved.

3.2. *Sensitivity analysis*

Here we investigate the sensitivity of the water ice dissipation dynamics to several key physical parameters. In the simulations for this section, we use the case from Section 3.1 as the baseline and modify only the parameters for sensitivity analysis, keeping all other parameters unchanged.

3.2.1. *Geothermal flux*

As compiled in Table 1, reported estimations for lunar geothermal heat flux (q_0) exhibit significant variance across the literature. To assess the impact of this uncertainty on our primary findings, we performed a sensitivity analysis using geothermal flux values spanning two orders of magnitude. We set the geothermal flux to 0.018 W/m^2 (Langseth et al., 1976a), 0.0018 W/m^2 (one order of magnitude lower than the typical

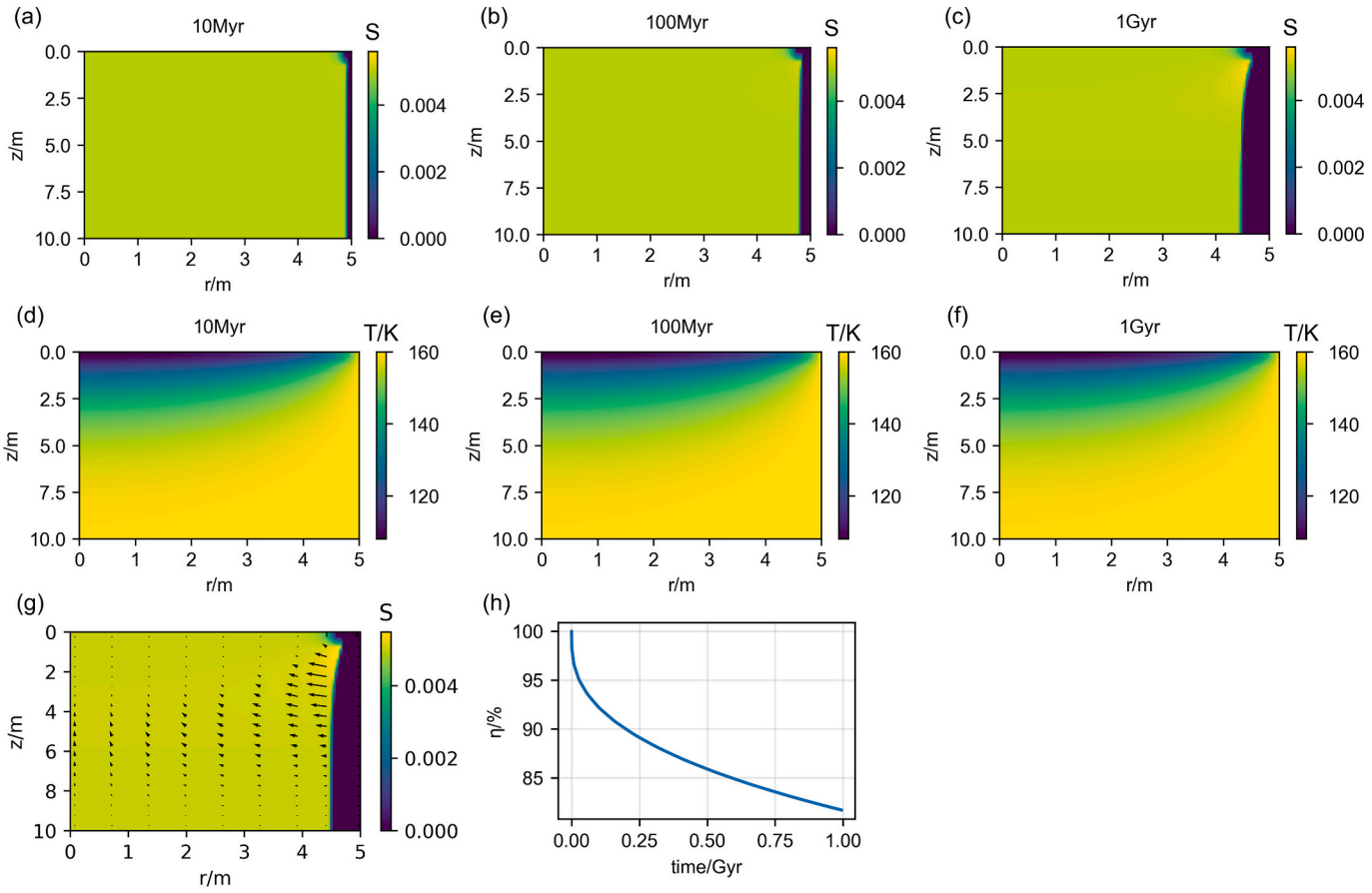

Fig. 3. The evolution of a typical micro cold trap initially containing a certain amount of uniformly distributed water ice over 1 billion years. The cold trap has a radius of 5 m and a depth of 10 m, with a radial boundary temperature of 160 K. The value of the average lunar regolith particle size divided by the tortuosity is set to 10^{-4} m. The upper boundary receives reflected or scattered solar radiation from the crater wall at 2.63 W/m^2. The initial water-ice saturation is 0.5%. The lunar geothermal heat flux is set to 0.018 W/m^2. No water-vapor influx from the exosphere is considered. (a, b, c) Spatial distributions of water-ice saturation at 10 Myr, 100 Myr, and 1 Gyr. (d, e, f) Temperature distributions at 10 Myr, 100 Myr, and 1 Gyr. (g) Arrows represent the spatial distribution of the water-ice mass-flux vector at a simulation time of 0.9 Gyr; arrow size indicates flux magnitude, overlaid on a heatmap of water-ice saturation. (h) Temporal evolution of the water-ice retention rate (η).

lunar value), and 0.067 W/m^2 (terrestrial heat flow data for the Earth,

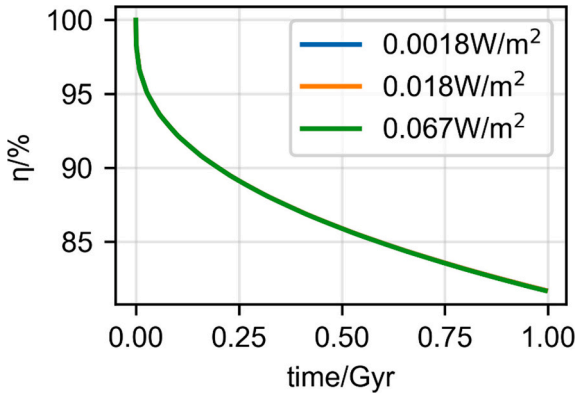

Fig. 4. The evolution of cold traps initially containing a certain amount of uniformly distributed water-ice. The cold trap has a radius of 5 m and a depth of 10 m, with a radial boundary temperature of 160 K. The value of the average lunar regolith particle size divided by the tortuosity is set to 10^{-4} m. The upper boundary receives reflected or scattered solar radiation from the crater wall at 2.63 W/m^2. The initial water-ice saturation is 0.5%. No water-vapor influx from the exosphere is considered. The curves show the water-ice retention rate (η) over time under different geothermal flux settings (0.0018 W/m^2, 0.018 W/m^2, 0.067 W/m^2).

(Lucazeau, 2019))), respectively. The resulting evolution of water ice retention rate (η) over time, illustrated in Fig. 4, demonstrates that the geothermal flux has almost no effect on the dynamics of water vapor evolution. Therefore, in following simulations, we always set $q_0 = 0.018$ W/m^2.

3.2.2. *Lateral boundary temperature*

The boundary temperature surrounding the cold trap is a crucial control on water ice retention. Observational data suggest that the annual average temperature at the edges of typical polar cold traps ranges between 120 K and 160 K (Williams et al., 2019). As shown in Fig. 5, simulations are conducted over 1 Gyr with the radial boundary temperature (T_{boundary}) set to 140 K, 160 K, and 180 K, while all other parameters are kept consistent with those in Section 3.1. The ice-loss rate is clearly highly sensitive to the boundary temperature: the cold trap with a boundary temperature of 140 K shows almost no water-ice loss, whereas the one at 180 K loses more than 60% of its initial ice. As illustrated in Fig. 5 (c), under high-temperature conditions the divergence in ice-loss rates at different depths becomes pronounced; in this scenario, only the surface layer retains appreciable water ice. This is consistent with the findings of (Talkington et al., 2022).

As discussed in Section 3.1, when the lateral boundary temperature is sufficiently high, a high-saturation belt forms at mild depth and near the ice front, due to inward mass transfer of water ice from the boundary region. This high-saturation belt is particularly evident under higher

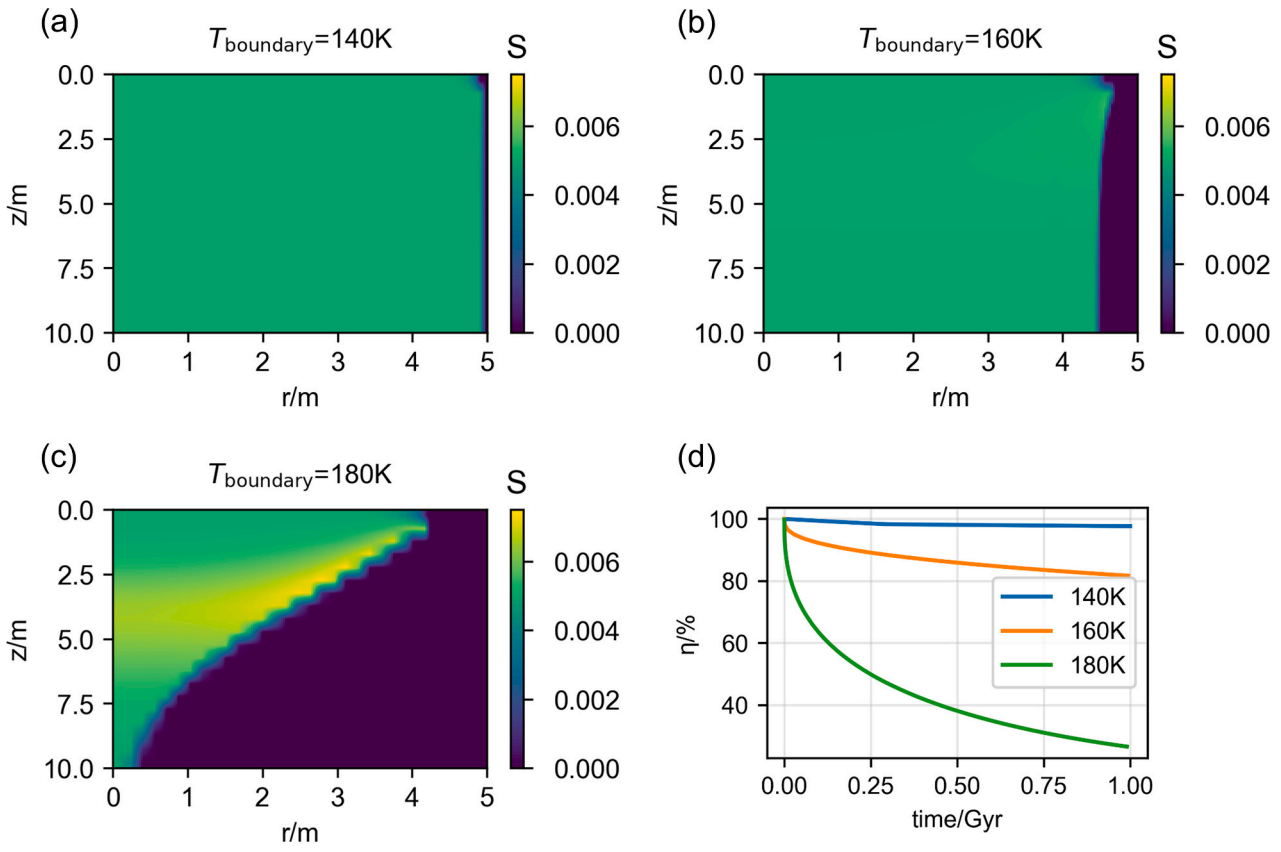

Fig. 5. The evolution of micro cold traps initially containing a certain amount of uniformly distributed water ice over 1 billion years. The cold trap has a radius of 5 m and a depth of 10 m. The value of the average lunar regolith particle size divided by the tortuosity is set to 10^{-4} m. The upper boundary receives reflected or scattered solar radiation from the crater wall at 2.63 W/m^2. The initial water-ice saturation is 0.5%. The lunar geothermal heat flux is set to 0.018 W/m^2. No water-vapor influx from the exosphere is considered. (a, b, c) Spatial distribution of water-ice saturation in the cold trap at a simulation time of 1 Gyr, with radial boundary temperatures set to 140 K, 160 K, and 180 K, respectively. (d) Temporal evolution of the cold-trap water-ice retention rate (η).

temperature, as shown in Fig. 5 (c).

3.2.3. *Initial saturation*

The initial water ice saturation is another critical factor. Based on the preceding analysis in Section 2, the initial saturation is considered to range from 0.1% to 10%. We set initial saturation S_{init} as 10%, 0.5% and 0.1%, and demonstrate the spatial distribution of ice saturation after 10^9 years in Fig. 6 (a)-(c), respectively. All other parameters are kept consistent with those in Section 3.1.

As shown in Fig. 6, the ice-loss rate and retention rate are strongly dependent on the initial saturation. Since the sublimation rate of water ice depends solely on temperature and the corresponding saturated vapor pressure, a cold trap with higher initial saturation experiences slower retreat of the ice front and thus attains a relatively higher retention rate. However, the proportional relationship between the retention rate and initial saturation in Fig. 6 (d) also indicates that cold traps with higher initial saturation experience a greater absolute mass loss of ice.

3.2.4. *Cold trap size*

The size of the cold trap, quantified by its radius, is a primary indicator for estimating potential water ice reserves. Observational estimates suggest that natural cold traps span an extensive range, from micro-scale traps with radii as small as 1 cm (Hayne et al., 2021) up to major features exceeding 20 km in diameter (Shackleton crater, (Halim et al., 2021)). However, traps significantly smaller than the meter scale often exhibit very short lifetimes due to the impact environment (Costello and Lucey, 2024). To assess the impact of scale on long-term retention, we investigate the evolution patterns of water ice within cold traps whose radii (R_c) range from 5 m to 100 m. All other parameters are kept consistent with those in Section 3.1.

As shown in the results of Fig. 7 (a-d), the ice-loss profiles along the edges are highly similar, and the retreat distances of the ice fronts are nearly identical. Consequently, larger cold traps achieve higher water-ice retention rates. Furthermore, the temperature distributions (Fig. 7 (e, f)) reveal that in large cold traps, only the peripheral regions reach temperatures sufficiently high to cause ice loss, while the extensive central low-temperature zone ($\langle 100\ K$) allows water ice to be preserved almost indefinitely.

3.2.5. *Effective diffusion coefficient*

The effective diffusion coefficient is governed by a characteristic length scale, namely the ratio of lunar regolith particle size to tortuosity (l_p/τ), which consequently influences the rate of water-ice loss. Based on (Grant et al., 1991), l_p is approximately 10^{-4} m, while τ typically ranges between 1 and 2 (Schieber et al., 2021). Accordingly, we performed simulations with l_p/τ set to 5×10^{-5} m, 1×10^{-4} m, and 2×10^{-4} m, respectively. All other parameters are kept consistent with those in Section 3.1.

The saturation distributions shown in Fig. 8 (a-c) indicate that a larger effective diffusion coefficient accelerates the loss of water ice. Fig. 8 (d) displays the temporal evolution of the water ice retention rate (η), which is inversely correlated with l_p/τ. Nevertheless, we notice that four times higher diffusion coefficient corresponds to less than two times higher dissipation, indicating the diffusion coefficient affect dissipation with a weak sublinear scaling.

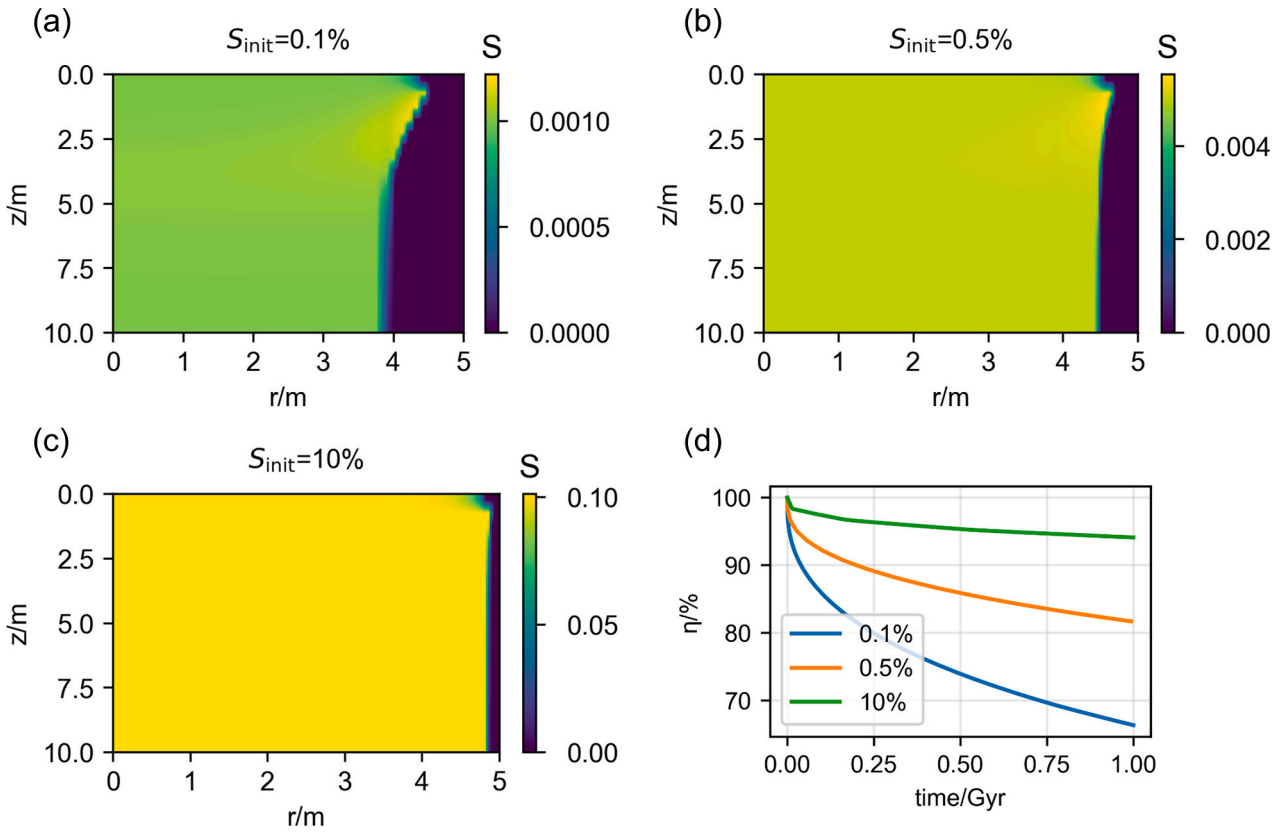

Fig. 6. The evolution of micro cold traps initially containing a certain amount of uniformly distributed water ice over 1 billion years. The cold trap has a radius of 5 m and a depth of 10 m, with a radial boundary temperature of 160 K. The value of the average lunar regolith particle size divided by the tortuosity is set to 10^{-4} m. The upper boundary receives reflected or scattered solar radiation from the crater wall at 2.63 W/m^2. The lunar geothermal heat flux is set to 0.018 W/m^2. No water-vapor influx from the exosphere is considered. (a, b, c) Spatial distribution of water-ice saturation in the cold trap at a simulation time of 1 Gyr, with initial water-ice saturations set to 0.1%, 0.5%, and 10%, respectively. (d) Temporal evolution of the cold-trap water-ice retention rate (η).

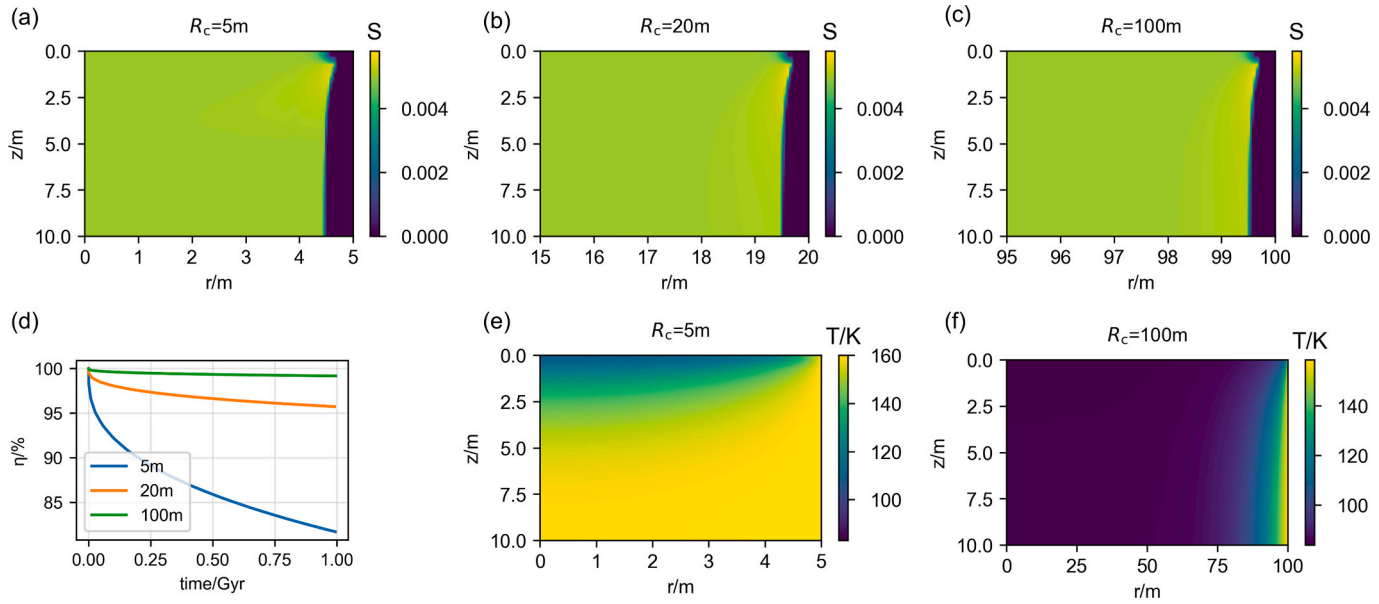

Fig. 7. The evolution of cold traps initially containing a certain amount of uniformly distributed water ice over 1 billion years. The cold trap has a depth of 10 m, with a radial boundary temperature of 160 K. The value of the average lunar regolith particle size divided by the tortuosity is set to 10^{-4} m. The upper boundary receives reflected or scattered solar radiation from the crater wall at 2.63 W/m^2. The initial water-ice saturation is 0.5%. The lunar geothermal heat flux is set to 0.018 W/m^2. No water-vapor influx from the exosphere is considered. (a, b, c) Spatial distribution of water-ice saturation in the cold trap at a simulation time of 1 Gyr, with radii set to 5 m, 20 m, and 100 m, respectively. (d) Temporal evolution of the cold-trap water-ice retention rate (η). (e, f) Spatial temperature distributions in the 5 m-radius and 100 m-radius cold traps at 1 Gyr.

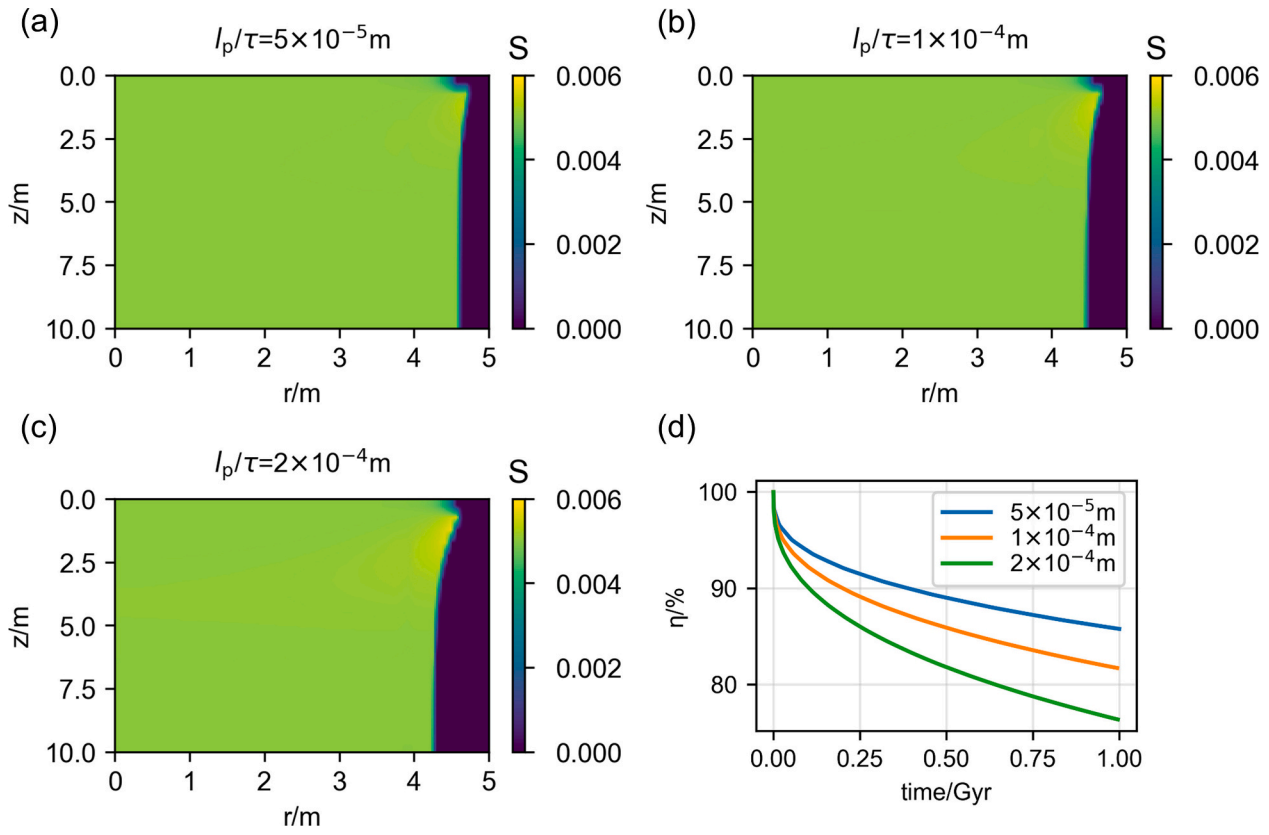

Fig. 8. The evolution of micro cold traps initially containing a certain amount of uniformly distributed water ice over 1 billion years. The cold trap has a radius of 5 m and a depth of 10 m, with a radial boundary temperature of 160 K. The upper boundary receives reflected or scattered solar radiation from the crater wall at 2.63 W/m^2. The initial water-ice saturation is 0.5%. The lunar geothermal heat flux is set to 0.018 W/m^2. No water-vapor influx from the exosphere is considered. (a, b, c) Spatial distribution of water-ice saturation in the cold trap at a simulation time of 1 Gyr, with the ratio of lunar regolith particle size to tortuosity (l_p/τ) set to 5 × 10^{-5} m, 1 × 10^{-4} m, and 2 × 10^{-4} m, respectively. (d) Temporal evolution of the cold-trap water-ice retention rate (η).

3.2.6. *Net external water vapor flux*

The magnitude of external water vapor flux is a major uncertainty affecting the total water ice reserves within the cold trap. In previous studies, estimations of the water vapor influx diffusing to the polar regions could differ by up to five orders of magnitude (J_{in} = 10^{-2}–10^3 kg·m^{-2}·Gyr^{-1}, Table 1). However, space-weathering processes such as meteoroid impacts can disrupt water ice in the surface layer of cold traps (Farrell et al., 2019; Morgan and Shemansky, 1991). Therefore, the lower limit of the net influx $J_{in,net}$ is taken as zero in our analysis.

As shown in Fig. 9, a small influx (e.g., 0.05 kg/m^2/Gyr, Fig. 9 (b)) does not alter the position of the ice front, and the ice loss in the subsurface remains essentially the same as in the no-influx case (Fig. 9 (a)). When the influx reaches 50 kg/m^2/Gyr (Fig. 9 (e)), the retreat of the ice front at top layer is noticeably slowed. With a sufficiently large influx (500 kg/m^2/Gyr, Fig. 9 (f)), a frost layer (S > 0.8) forms at the surface. In addition, due to the minimal mass transfer between the top layer and the underlying layers (Section 3.1), the vapor influx does not affect the ice front at the bottom, as shown in Supplementary Material Fig. S2.

We note that thick icy layer (as that with S > 0.8) does not match current observation (Kereszturi, 2023). This suggests that estimates of J_{in} exceeding 500 kg/m^2/Gyr may be too high, or that the effects of space weathering have been underestimated.

A question therefore arises: can we distinguish the ice from external vapor influx and the initially formed ice? To answer this question, we analyze the net water vapor flux at 0.5-m subsurface depth ($J_{z=0.5m}$), and calculate its ratio to that of $J_{in,net}$, shown in Fig. 9(h). The results demonstrate that the magnitude of $J_{z=0.5m}$ is negligible when compared to $J_{in,net}$ if $J_{in,net}$ > 0.5 kg/m^2/Gyr, indicating minimal exchange between interior and exterior water ice. This phenomenon suggests that the water ice in shallow lunar regolith and deep regolith likely exhibits significant physicochemical differences due to distinct origins.

3.2.7. *Radiative flux from crater wall*

The radiative flux from the crater wall, q_{wall}, is a key factor controlling water ice retention. Based on calculations from Supplementary Material S6, q_{wall} in high-latitude craters can range from 0.86 to 4.83 W/m^2. Multiple scenarios are simulated by setting q_{wall} to 0.86 W/m^2, 2.63 W/m^2, and 4.83 W/m^2. All other parameters are kept consistent with those in Section 3.1.

In absence of external water vapor influx, ice-loss rate is very weakly correlated with the radiative flux from the crater wall, as shown in Fig. 10 (a-d). However, when there is a net water-vapor influx $J_{in,net}$ = 5 kg/m^2/Gyr, as presented in Fig. 10 (e-h), q_{wall} exerts a stronger influence on the top layer of the water ice. When an external vapor influx is present at the surface, q_{wall} has a more pronounced impact on the overall ice retention rate.

4. Implications and limitations

4.1. *Reserve prediction*

Based on the aforementioned simulation results, we analyze the factors influencing the retention rate of water ice in cold traps. In this section, we show comprehensive results to show prediction of ice reserve under different PSR size (R_c), initial saturation (S_{init}) and boundary temperature ($T_{boundary}$).

As shown in Fig. 11, we plot heat maps of the water-ice retention rate (η) as a function of cold-trap radius (R_c) versus initial saturation (S_{init}),

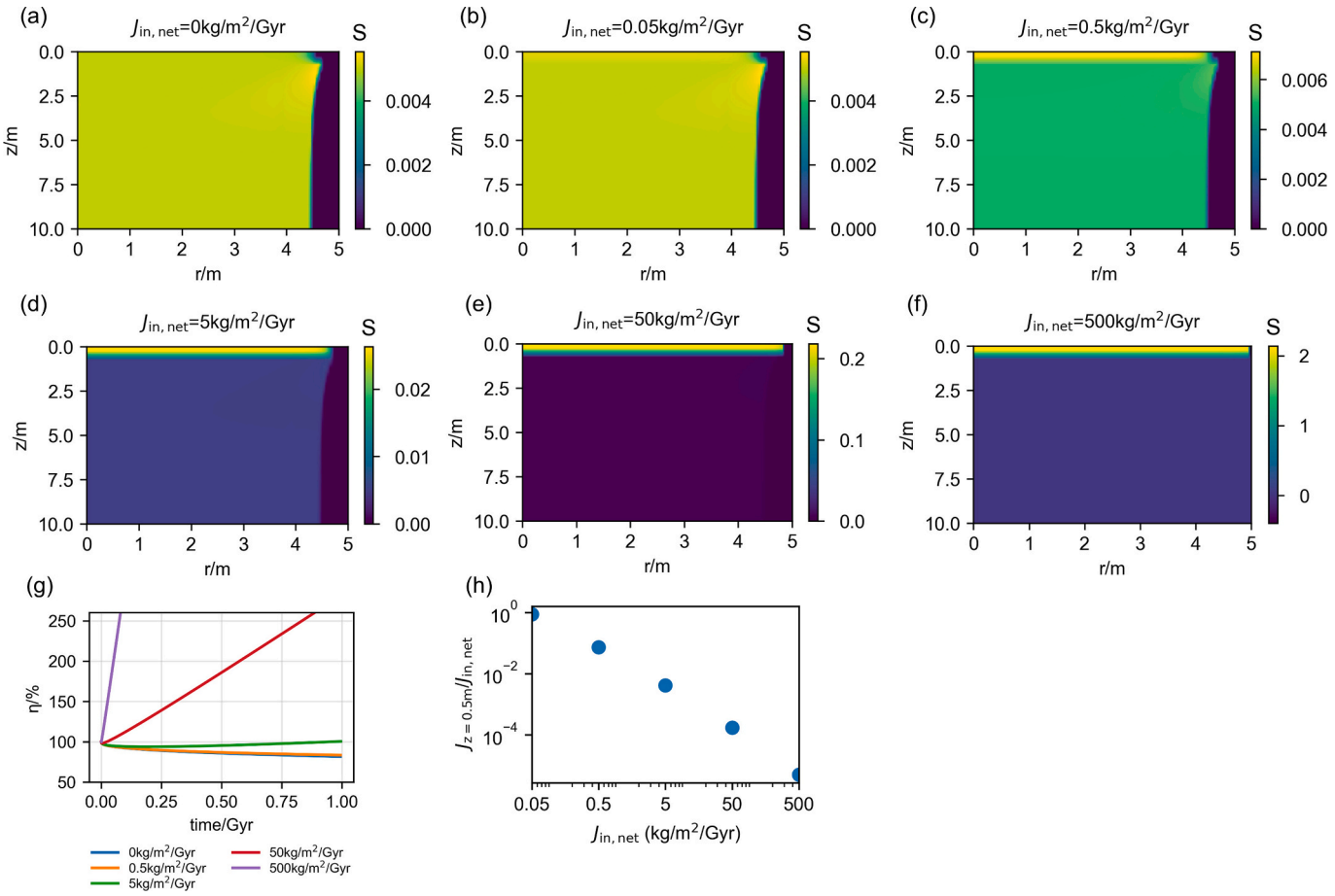

Fig. 9. The evolution of micro cold traps initially containing a certain amount of uniformly distributed water ice over 1 billion years. The cold trap has a radius of 5 m and a depth of 10 m, with a radial boundary temperature of 160 K. The value of the average lunar regolith particle size divided by the tortuosity is set to 10^{-4} m. The upper boundary receives reflected or scattered solar radiation from the crater wall at 2.63 W/m^2. The initial water-ice saturation is 0.5%. The lunar geothermal heat flux is set to 0.018 W/m^2. (a, b, c, d, e, f) Spatial distribution of water-ice saturation in the cold trap at a simulation time of 1 Gyr, with the net water-vapor influx $J_{in,net}$ set to 0, 0.05 kg/m^2/Gyr, 0.5 kg/m^2/Gyr, 5 kg/m^2/Gyr, 50 kg/m^2/Gyr, and 500 kg/m^2/Gyr, respectively. (g) Temporal evolution of the cold-trap water-ice retention rate (η). (h) The ratio of the time-averaged ice mass transfer between the top regolith layer (0–0.5 m) and the underlying layer $J_{z=0.5m}$, (in kg·m^{-2}·Gyr^{-1}) to the net influx from the exosphere $J_{in,net}$ (in kg·m^{-2}·Gyr^{-1}) as a function of the latter.

and as a function of radial boundary temperature ($T_{boundary}$) versus initial saturation (S_{init}). Contour lines corresponding to η = 30%, 50%, and 90% are overlaid. All other simulation conditions are the same as in Section 3.1. Detailed numerical values are provided in Supplementary Materials Tables 1 and 2. We can employ η as a quantitative criterion to estimate the ranges of radius, initial saturation, and radial boundary temperature for cold traps that possess practical value for large-scale water extraction. For example, cold traps with radii larger than 20 m or radial boundary temperatures below 140 K exhibit $\eta > 90\%$.

4.2. Limited vertical mixing

Surface ice frost layer may provide valuable information about the surrounding environment (Rubanenko, 2024). For example, the frost thickness is directly connected to water vapor influx at the surface, which may indicate the historical intensity of solar wind and past impact events. Under given geological conditions, the thickness of lunar surface water ice can be used to estimate both the cold trap evolution timescale and the average surface vapor influx.

In addition, we note that the temperature of the upper layer is so low that water vapor migration downward is negligible as shown in Fig. 9 (h). The external vapor accumulates only at the top 0.5 m layer (Fig. 9 (e-f)), with limited mixing with regolith by the gardening effect.

There may be a geochemically plausible implication: if we get samples from both the upper layer and deep regolith, they should be poorly mixed before and thus should have completely different sources. This separation may provide richer information than previously expected.

4.3. Limitations

To allow fast calculation with acceptable accuracy, the simulations are of some major limitations. Some limitations can be addressed by incorporating more existing data and investing more computational resources:

- we simplify the shape of PSRs as a thin cylinder, while real PSRs are of more complex geometry;
- we adopt uniform porosity and permeability distribution in the regolith, while there is variation in both vertical and horizontal directions;

However, some limitations need future investigations on lunar samples, new lunar missions and more remote sensing data to overcome:

- the interaction between water ice and regolith particles may be oversimplified, while realistic ice-regolith interaction is not fully resolved;

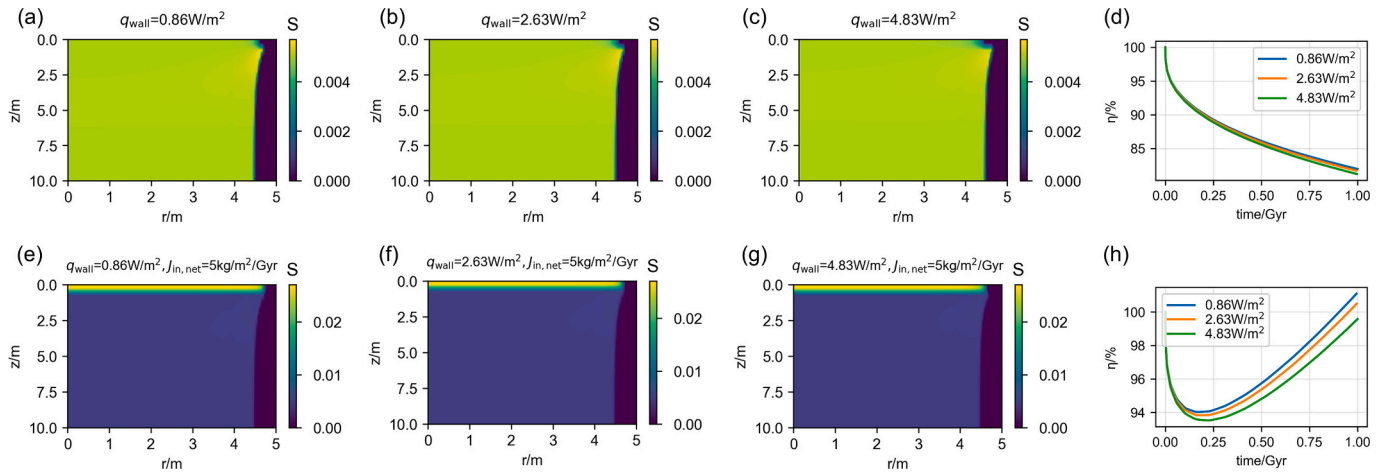

Fig. 10. The evolution of micro cold traps initially containing a certain amount of uniformly distributed water ice over 1 billion years. The cold trap has a radius of 5 m and a depth of 10 m, with a radial boundary temperature of 160 K. The value of the average lunar regolith particle size divided by the tortuosity is set to 10^{-4} m. The initial water-ice saturation is 0.5%. The lunar geothermal heat flux is set to 0.018 W/m^2. (a, b, c) Spatial distribution of water-ice saturation in the cold trap at a simulation time of 1 Gyr, with radiative flux from the crater wall set to 0.86 W/m^2, 2.63 W/m^2, and 4.83 W/m^2, respectively. No water-vapor influx from the exosphere is considered. (d) Temporal evolution of the cold-trap water-ice retention rate (η). (e, f, g) Spatial distribution of water-ice saturation in the cold trap at a simulation time of 1 Gyr, with radiative flux from the crater wall set to 0.86 W/m^2, 2.63 W/m^2, and 4.83 W/m^2, respectively. The net water-vapor influx $J_{in,net}$ is fixed at 5 kg/m^2/Gyr. (h) Temporal evolution of the cold-trap water-ice retention rate (η) under the condition that the net water-vapor influx $J_{in,net}$ is set to 5 kg/m^2/Gyr.

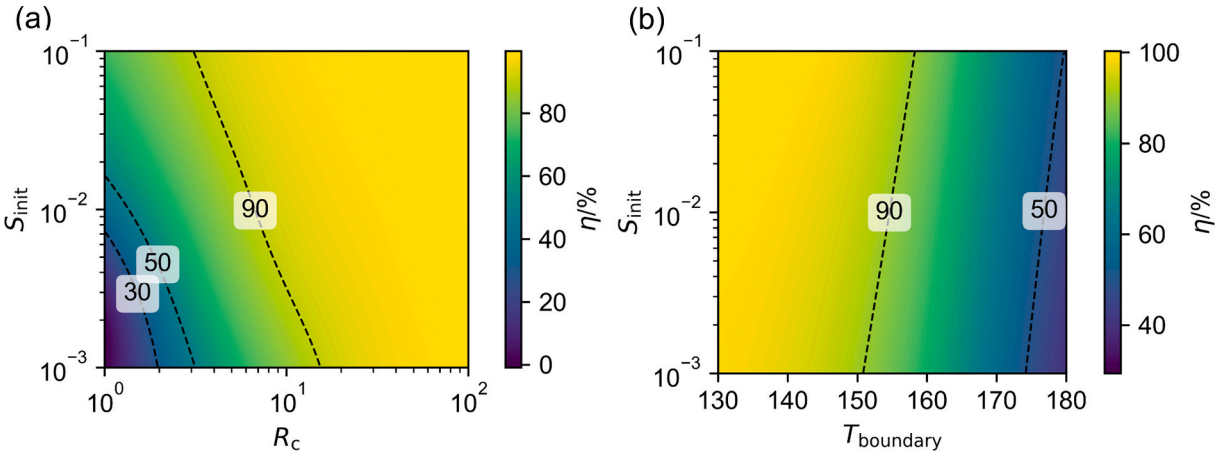

Fig. 11. Water-ice retention over 1 billion years heat maps for cold traps initially containing a certain amount of uniformly distributed water ice. The cold trap has a depth of 10 m. The value of the average lunar regolith particle size divided by the tortuosity is set to 10^{-4} m. The upper boundary receives reflected or scattered solar radiation from the crater wall at 2.63 W/m^2. The lunar geothermal heat flux is set to 0.018 W/m^2. No water-vapor influx from the exosphere is considered. Contour lines mark η = 30%, 50%, and 90%. (a) Retention rate η as a function of cold-trap radius (R_c) and initial ice saturation (S_{init}) under a fixed radial boundary temperature of 160 K. (b) η as a function of radial boundary temperature ($T_{boundary}$) and S_{init} for a cold-trap radius of 5 m.

- we assume that the top 0.5 m layer is uniform due to gardening effect and the influx can be fully mixed with shallow layer in geologically short time, which needs further validation;
- we do not count for the water dissipation by external disturbances such as electrostatic fields, solar wind bombardment, and micro-meteorite impacts.

5. Conclusions

In this work, we investigate the impact of various geological variables on the retention ratio of water ice by constructing a comprehensive model for the evolution of water ice in the PSRs of the lunar polar regions. We propose a model for water ice evolution that incorporates chemical potential gradients as the mass transfer driving force. The model highlights the influence of lateral temperature differences on water ice distribution. We demonstrate the correlation between water ice distribution and PSRs sizes, boundary temperature, initial ice saturation, effective diffusion coefficient, the water vapor influx, and the reflected and scatted solar radiation from crater wall.

The main conclusions of this work include:

1) Cold trap size, boundary temperature, initial ice saturation, regolith particle size and water vapor influx from lower latitudes have significant effects on ice distribution evolution over 1 billion years in PSRs. In contrast, gravitational effect, surface energy, latent heat for ice phase change and geothermal flux have negligible effect.
2) In cold traps with radii greater than 20 m, the water ice retention ratio exceeds 90%, and the ice distribution evolution near the side boundary is insensitive to cold trap size. In contrast, water ice within cold traps with a radius smaller than 1 m may completely dissipate.
3) The intensity of water vapor influx from lower latitudes determines the ice-bearing layer on the cold trap surface. When the net water

vapor influx exceeds 5 kg/m^2/Gyr, the shallow regolith ice accumulation can effectively compensate the escape of water ice from the edge in a 5-m cold trap. The influx J_{in} is unlikely to be larger than 500 kg/m^2/Gyr unless gardening effect results in major mass loss. The vertical mass exchange between shallow regolith and deeper regolith at half meter depth is extremely low, indicating that ice in shallow regolith and deep regolith in PSRs may have distinct origins and are not necessarily relevant.

This work provides a framework to analyze the evolution of water ice and other volatile in lunar PSRs and other similar geological structures, and contribute to future in-situ water ice utilization for lunar bases.

Open research

The supplementary material and associated videos for this manuscript can be downloaded from a public repository of research data, Zenodo, through the link:
https://zenodo.org/records/16413020

CRediT authorship contribution statement

Sunpeng Zhou: Writing – review & editing, Validation, Investigation, Data curation. **Zhenpeng Wang:** Writing – review & editing, Writing – original draft, Software, Investigation, Formal analysis. **Shanshan Zhou:** Data curation. **Hang Deng:** Writing – review & editing. **Qinggong Wang:** Data curation, Writing – review & editing. **Rui Wu:** Software. **Wei Yao:** Resources. **Ke Xu:** Writing – review & editing, Validation, Supervision, Resources, Project administration, Methodology, Funding acquisition, Conceptualization.

Declaration of competing interest

The authors declare that they have no known competing financial interests or personal relationships that could have appeared to influence the work reported in this paper.

Acknowledgments

This work was supported by the National Key Research and Development Program of China (No: 2021YFA0717200) and the National Natural Science Foundation of China (No. U23B6004). Authors acknowledge the support from Chang'e-7 Science team.

Appendix A. Supplementary data

Supplementary data to this article can be found online at https://doi.org/10.1016/j.icarus.2026.117022.

Data availability

Data will be made available on request.

References

Angelopoulos, V., 2011. The ARTEMIS Mission. Space Sci. Rev. 165 (1), 3–25. https://doi.org/10.1007/s11214-010-9687-2.
Arnold, J.R., 1979. Ice in the lunar POLAR regions. J. Geophys. Res. 84 (NB10), 5659–5668. https://doi.org/10.1029/JB084iB10p05659.
Bandfield, J.L., Hayne, P., Williams, J.P., Greenhagen, B.T., Paige, D.A., 2015. Lunar surface roughness derived from LRO diviner radiometer observations. Icarus 248, 357–372. https://doi.org/10.1016/j.icarus.2014.11.009.
Cannon, K.M., Deutsch, A.N., Head, J.W., Britt, D.T., 2020. Stratigraphy of ice and ejecta deposits at the lunar poles. Geophys. Res. Lett. 47 (21), e2020GL088920. https://doi.org/10.1029/2020gl088920.
de Chalendar, J.A., Garing, C., Benson, S.M., 2019. Pore-scale modelling of Ostwald ripening (vol 835, pg 363, 2018). J. Fluid Mech. 866, 929. https://doi.org/10.1017/jfm.2019.180.
Chen, J., Xie, L., Li, L., Liu, Y., Zhang, A., Zhang, Y., Li, J., Xu, Y., Wang, J., Yang, Y., Zhou, B., Yan, Q., Xu, Q., Gou, X., Feng, Y., Zhong, T., Wang, C., 2025. Monte Carlo simulation of the global migration of lunar hydroxyl from a magnetic-shielded solar wind source. J. Geophys. Res.: Planets 130 (8), e2025JE009003. https://doi.org/10.1029/2025JE009003.
Colaprete, A., Schultz, P., Heldmann, J., Wooden, D., Shirley, M., Ennico, K., Hermalyn, B., Marshall, W., Ricco, A., Elphic, R.C., Goldstein, D., Summy, D., Bart, G.D., Asphaug, E., Korycansky, D., Landis, D., Sollitt, L., 2010. Detection of water in the LCROSS ejecta plume. Science 330 (6003), 463–468. https://doi.org/10.1126/science.1186986.
Costello, E.S., Lucey, P.G., 2024. The age and evolution of lunar Micro cold traps at the scale of surface exploration. Geophys. Res. Lett. 51 (1), e2023GL105369. https://doi.org/10.1029/2023GL105369.
Costello, E.S., Ghent, R.R., Lucey, P.G., 2018. The mixing of lunar regolith: vital updates to a canonical model. Icarus 314, 327–344. https://doi.org/10.1016/j.icarus.2018.05.023.
Costello, E.S., Ghent, R.R., Hirabayashi, M., Lucey, P.G., 2020. Impact gardening as a constraint on the age, source, and evolution of ice on mercury and the moon. J. Geophys. Res. Planets 125 (3), e2019JE006172. https://doi.org/10.1029/2019je006172.
Crider, D.H., Vondrak, R.R., 2000. The solar wind as a possible source of lunar polar hydrogen deposits. J. Geophys. Res.-Planets 105 (E11), 26773–26782. https://doi.org/10.1029/2000je001277.
Crider, D.H., Vondrak, R.R., 2003. Space weathering effects on lunar cold trap deposits. J. Geophys. Res. Planets 108 (E7), 5079. https://doi.org/10.1029/2002je002030.
Danque, H.A., Cannon, K.M., 2024. Lunar polar volatile remobilization in regolith-filled craters. Icarus 411, 115953. https://doi.org/10.1016/j.icarus.2024.115953.
Daucik, K., Dooley, R., 2011. Revised Release on the Pressure along the Melting and Sublimation Curves of Ordinary Water Substance. Release R14–08.
Fa, W., 2020. Bulk density of the lunar regolith at the Chang'E-3 landing site as estimated from lunar penetrating radar. Earth Space Sci. 7 (2), e2019EA000801. https://doi.org/10.1029/2019EA000801.
Farrell, W.M., Hurley, D.M., Poston, M.J., Hayne, P.O., Szalay, J.R., McLain, J.L., 2019. The young age of the LAMP-observed frost in lunar polar cold traps. Geophys. Res. Lett. 46 (15), 8680–8688. https://doi.org/10.1029/2019GL083158.
Feng, Y.T., Wang, C.X., Jin, X., Xu, K., 2022. Comprehensive Darcy-scale analysis of ripening in porous media. Transp. Porous Media 144 (1), 301–316. https://doi.org/10.1007/s11242-022-01794-4.
Goswami, J.N., Annadurai, M., 2011. Chandrayaan-2 Mission. 42nd Annual Lunar and Planetary Science Conference.
Grant, H., Heiken, D., T., V., Bevan, M., French, 1991. Lunar Sourcebook: A User's Guide to the Moon.
Grott, M., Knollenberg, J., Krause, C., 2010. Apollo lunar heat flow experiment revisited: A critical reassessment of the in situ thermal conductivity determination. J. Geophys. Res.: Planets 115 (E11). https://doi.org/10.1029/2010JE003612.
Halim, S.H., Barrett, N., Boazman, S.J., Gawronska, A.J., Gilmour, C.M., Harish, McCanaan, K., Satyakumar, A.V., Shah, J., Kring, D.A., 2021. Numerical modeling of the formation of Shackleton crater at the lunar south pole. Icarus 354, 113992. https://doi.org/10.1016/j.icarus.2020.113992.
Hayne, P.O., Bandfield, J.L., Siegler, M.A., Vasavada, A.R., Ghent, R.R., Williams, J.P., Greenhagen, B.T., Aharonson, O., Elder, C.M., Lucey, P.G., Paige, D.A., 2017. Global regolith thermophysical properties of the moon from the diviner lunar radiometer experiment. J. Geophys. Res.-Planets 122 (12), 2371–2400. https://doi.org/10.1002/2017je005387.
Hayne, P.O., Aharonson, O., Schörghofer, N., 2021. Micro cold traps on the moon. Nat. Astron. 5 (2), 169–175. https://doi.org/10.1038/s41550-020-1198-9.
He, H., Ji, J., Zhang, Y., Hu, S., Lin, Y., Hui, H., Hao, J., Li, R., Yang, W., Tian, H., Zhang, C., Anand, M., Tartèse, R., Gu, L., Li, J., Zhang, D., Mao, Q., Jia, L., Li, X., Wu, F., 2023. A solar wind-derived water reservoir on the moon hosted by impact glass beads. Nat. Geosci. 16 (4), 294–300. https://doi.org/10.1038/s41561-023-01159-6.
Head, J.W., Wilson, L., Deutsch, A.N., Rutherford, M.J., Saal, A.E., 2020. Volcanically induced transient atmospheres on the moon: assessment of duration, significance, and contributions to polar volatile traps. Geophys. Res. Lett. 47 (18), e2020GL089509. https://doi.org/10.1029/2020GL089509.
Heiken, G.H., Vaniman, D.T., French, B.M., 1991. Lunar Sourcebook, a User's Guide to the Moon. Cambridge University Press.
Huang, Z.Y., Nomura, K., Morrissey, L.S., Wang, J., 2022. Molecular dynamics simulation of solar wind implantation in the permanently shadowed regions on the lunar surface. Geophys. Res. Lett. 49 (18), e2022GL099333. https://doi.org/10.1029/2022gl099333.
Ivanov, B.A., 2001. Mars/moon cratering rate ratio estimates. Space Sci. Rev. 96 (1–4), 87–104. https://doi.org/10.1023/a:1011941121102.
Jones, B.M., Aleksandrov, A., Hibbitts, K., Dyar, M.D., Orlando, T.M., 2018. Solar wind-induced water cycle on the moon. Geophys. Res. Lett. 45 (20), 10959–10967. https://doi.org/10.1029/2018gl080008.
Kereszturi, A., 2023. Polar ice on the moon. In: Cudnik, B. (Ed.), Encyclopedia of Lunar Science. Springer International Publishing, pp. 971–980. https://doi.org/10.1007/978-3-319-14541-9_216.
Krevor, S., Blunt, M.J., Benson, S.M., Pentland, C.H., Reynolds, C., Al-Menhali, A., Niu, B., 2015. Capillary trapping for geologic carbon dioxide storage – from pore scale physics to field scale implications. Int. J. Greenh. Gas Con. 40, 221–237. https://doi.org/10.1016/j.ijggc.2015.04.006.
Langseth, M.G., Keihm, S.J., Peters, K., 1976. Revised lunar heat-flow values. In: Lunar Science Conference, 7th, Houston, Tex., March 15-19, 1976, Proceedings. Volume 3. (A77-34651 15-91). Pergamon Press, Inc, New York, pp. 3143–3171.

Levenspiel, O., 2014. Combination of heat transfer resistances. In: Levenspiel, O. (Ed.), Engineering Flow and Heat Exchange. Springer US, pp. 211–221. https://doi.org/10.1007/978-1-4899-7454-9_10.

Li, S., Lucey, P.G., Milliken, R.E., Hayne, P.O., Fisher, E., Williams, J.P., Hurley, D.M., Elphic, R.C., 2018. Direct evidence of surface exposed water ice in the lunar polar regions. Proc. Natl. Acad. Sci. USA 115 (36), 8907–8912. https://doi.org/10.1073/pnas.1802345115.

Li, Y., Garing, C., Benson, S.M., 2020. A continuum-scale representation of Ostwald ripening in heterogeneous porous media. J. Fluid Mech. 889, A14.

Logan, L.M., Hunt, G.R., Balsamo, S.R., Salisbury, J.W., 1972. Midinfrared emission spectra of Apollo 14 and 15 soils and remote compositional mapping of the moon. Proc. Lunar Sci. Conf. 3, 3069.

Lucazeau, F., 2019. Analysis and mapping of an updated terrestrial heat flow data set. Geochem. Geophys. Geosyst. 20 (8), 4001–4024. https://doi.org/10.1029/2019GC008389.

Luchsinger, K.M., Chanover, N.J., 2022. Seasons of ice: water ice migration and seasonal transient shadow at the lunar poles. J. Geophys. Res.: Planets 127 (10), e2022JE007336. https://doi.org/10.1029/2022JE007336.

Moores, J.E., 2016. Lunar water migration in the interval between large impacts: heterogeneous delivery to permanently shadowed regions, fractionation, and diffusive barriers. J. Geophys. Res.: Planets 121 (1), 46–60. https://doi.org/10.1002/2015JE004929.

Morgan, T.H., Shemansky, D.E., 1991. Limits to the lunar atmosphere. J. Geophys. Res. Space Physics 96 (A2), 1351–1367. https://doi.org/10.1029/90JA02127.

Ong, L., Asphaug, E.I., Korycansky, D., Coker, R.F., 2010. Volatile retention from cometary impacts on the moon. Icarus 207 (2), 578–589. https://doi.org/10.1016/j.icarus.2009.12.012.

Paige, D.A., Siegler, M.A., Zhang, J.A., Hayne, P.O., Foote, E.J., Bennett, K.A., Vasavada, A.R., Greenhagen, B.T., Schofield, J.T., McCleese, D.J., Foote, M.C., DeJong, E., Bills, B.G., Hartford, W., Murray, B.C., Allen, C.C., Snook, K., Soderblom, L.A., Calcutt, S., Lucey, P.G., 2010. Diviner lunar radiometer observations of cold traps in the moon's south polar region. Science 330 (6003), 479–482. https://doi.org/10.1126/science.1187726.

Parzinger, S., 2014. Analytische Modellierung der temperatur-und gasdruckabhängigen effektiven Wärmeleitfähigkeit von Pulvern. Verlag Dr. Hut.

Ratcliffe, E., 1962. The thermal conductivity of ice new data on the temperature coefficient. Philos. Mag. 7 (79), 1197–1203.

Reinecke, S.A., Sleep, B.E., 2002. Knudsen diffusion, gas permeability, and water content in an unconsolidated porous medium. Water Resour. Res. 38 (12), 1280. https://doi.org/10.1029/2002wr001278.

Reiss, P., 2018. A combined model of heat and mass transfer for the in situ extraction of volatile water from lunar regolith. Icarus 306, 1–15. https://doi.org/10.1016/j.icarus.2018.01.020.

Rubanenko, L., 2024. The ephemeral state of ice in micro cold traps on the moon. Icarus 421, 116199. https://doi.org/10.1016/j.icarus.2024.116199.

Rubanenko, L., Aharonson, O., 2017. Stability of ice on the moon with rough topography. Icarus 296, 99–109. https://doi.org/10.1016/j.icarus.2017.05.028.

Rubanenko, L., Venkatraman, J., Paige, D.A., 2019. Thick ice deposits in shallow simple craters on the moon and mercury. Nat. Geosci. 12 (8), 597–601. https://doi.org/10.1038/s41561-019-0405-8.

Schieber, G.L., Jones, B.M., Orlando, T.M., Loutzenhiser, P.G., 2021. Characterization of H2O transport through Johnson Space Center number 1A lunar regolith simulant at low pressure for in-situ resource utilization. Phys. Fluids 33 (3), 037117. https://doi.org/10.1063/5.0042589.

Schieber, G.L., Jones, B.M., Orlando, T.M., Loutzenhiser, P.G., 2022. Indirect solar receiver development for the thermal extraction of H2O(v) from lunar regolith: heat and mass transfer modeling. Acta Astronaut. 190, 365–376. https://doi.org/10.1016/j.actaastro.2021.09.020.

Schörghofer, N., 2025. Diffusion-adsorption of water vapor in chemically activated lunar soil. Planet. Sci. J. 6 (7), 164. https://doi.org/10.3847/PSJ/ade5b2.

Schörghofer, N., Rufu, R., 2023. Past extent of lunar permanently shadowed areas. *Science*. Advances 9 (37), eadh4302. https://doi.org/10.1126/sciadv.adh4302.

Schorghofer, N., Taylor, G.J., 2007. Subsurface migration of H2O at lunar cold traps. J. Geophys. Res.: Planets 112 (E2). https://doi.org/10.1029/2006JE002779.

Schultz, P.H., Hermalyn, B., Colaprete, A., Ennico, K., Shirley, M., Marshall, W.S., 2010. The LCROSS cratering experiment. Science 330 (6003), 468–472. https://doi.org/10.1126/science.1187454.

Siegler, M., Aharonson, O., Carey, E., Choukroun, M., Hudson, T., Schorghofer, N., Xu, S., 2012. Measurements of thermal properties of icy Mars regolith analogs. J. Geophys. Res. Planets 117, E03001. https://doi.org/10.1029/2011je003938.

Siegler, M., Paige, D., Williams, J.P., Bills, B., 2015. Evolution of lunar polar ice stability. Icarus 255, 78–87. https://doi.org/10.1016/j.icarus.2014.09.037.

Siegler, M.A., Bills, B.G., Paige, D.A., 2011. Effects of orbital evolution on lunar ice stability. J. Geophys. Res. 116, E03010. https://doi.org/10.1029/2010je003652.

Song, H., Zhang, J., Ni, D., Sun, Y., Zheng, Y., Kou, J., Zhang, X., Li, Z., 2021. Investigation on in-situ water ice recovery considering energy efficiency at the lunar south pole. Appl. Energy 298, 117136. https://doi.org/10.1016/j.apenergy.2021.117136.

Spudis, P.D., Bussey, B., Plescia, J., Josset, J.L., Beauvivre, S., 2008. Geology of Shackleton Crater and the south pole of the Moon. Geophys. Res. Lett. 35 (14), L14201. https://doi.org/10.1029/2008gl034468.

Stewart, B.D., Pierazzo, E., Goldstein, D.B., Varghese, P.L., Trafton, L.M., 2011. Simulations of a comet impact on the moon and associated ice deposition in polar cold traps. Icarus 215 (1), 1–16. https://doi.org/10.1016/j.icarus.2011.03.014.

Talkington, C.L., Hirabayashi, M., Montalvo, P.E., Deutsch, A.N., Fassett, C.I., Siegler, M. A., Shepherd, S.L., King Jr., D.T., 2022. Survival of ancient lunar water affected by topographic degradation of old, large complex craters. Geophys. Res. Lett. 49 (15), e2022GL099241. https://doi.org/10.1029/2022GL099241.

Vasavada, A.R., Paige, D.A., Wood, S.E., 1999. Near-surface temperatures on mercury and the moon and the stability of polar ice deposits. Icarus 141 (2), 179–193. https://doi.org/10.1006/icar.1999.6175.

Watson, K., Murray, B.C., Brown, H., 1961. The behavior of volatiles on the lunar surface. J. Geophys. Res. 66 (9), 3033–3045. https://doi.org/10.1029/jz066i009p03033.

Wei, G., Li, X., Gan, H., Shi, Y., 2023. Retrieval of lunar polar heat flow from Chang'E-2 microwave radiometer and diviner observations [original research]. Front. Astron. Space Sci. 10. https://doi.org/10.3389/fspas.2023.1179558.

Wilcoski, A.X., Hayne, P.O., Landis, M.E., 2022. Polar ice accumulation from volcanically induced transient atmospheres on the moon. Planet. Sci. J. 3 (5), 99. https://doi.org/10.3847/PSJ/ac649c.

Williams, J.P., Greenhagen, B.T., Paige, D.A., Schorghofer, N., Sefton-Nash, E., Hayne, P. O., Lucey, P.G., Siegler, M.A., Aye, K.M., 2019. Seasonal polar temperatures on the moon. J. Geophys. Res.-Planets 124 (10), 2505–2521. https://doi.org/10.1029/2019je006028.

Woods-Robinson, R., Siegler, M.A., Paige, D.A., 2019. A model for the Thermophysical properties of lunar regolith at low temperatures. J. Geophys. Res.: Planets 124 (7), 1989–2011. https://doi.org/10.1029/2019JE005955.

Wu, B., Wang, Y., Werner, S.C., Prieur, N.C., Xiao, Z., 2022. A global analysis of crater depth/diameter ratios on the moon. Geophys. Res. Lett. 49 (20), e2022GL100886. https://doi.org/10.1029/2022GL100886.

Xu, K., Mehmani, Y., Shang, L., Xiong, Q., 2019. Gravity-induced bubble ripening in porous media and its impact on capillary trapping stability. Geophys. Res. Lett. 46 (23), 13804–13813. https://doi.org/10.1029/2019GL085175.

Yu, Y.H.J., Wang, C.X., Liu, J.N., Mao, S., Mehmani, Y., Xu, K., 2023. Bubble coarsening kinetics in porous media. Geophys. Res. Lett. 50 (1). https://doi.org/10.1029/2022gl100757.

Zheng, Q., Xu, J., Yang, B., Yu, B., 2013. Research on the effective gas diffusion coefficient in dry porous media embedded with a fractal-like tree network. Phys. A: Statist. Mech. Appl. 392 (6), 1557–1566. https://doi.org/10.1016/j.physa.2012.12.003.

Zhong, Z., Yan, J., He, H., Wen, Q., Liu, D., Barriot, J.-P., 2023. Illumination and regolith temperature at China's next candidate lunar landing site Shackleton crater. Sci. China Earth Sci. 66 (2), 417–429. https://doi.org/10.1007/s11430-022-9992-4.